

Temporal variations of solar inertial mode parameters from GONG (2002–2024) and HMI (2010–2024)

Rossby modes ($3 \leq m \leq 16$) and $m = 1$ high-latitude mode

B Lekshmi^{1,2}, Zhi-Chao Liang¹, Laurent Gizon^{1,3,4,*}, Jordan Philidet⁵, and Kiran Jain²

¹ Max-Planck-Institut für Sonnensystemforschung, Justus-von-Liebig-Weg 3, 37077 Göttingen, Germany

² National Solar Observatory, Boulder, CO 80303, USA

³ Institut für Astrophysik und Geophysik, Georg-August-Universität Göttingen, 37077 Göttingen, Germany

⁴ Center for Astrophysics and Space Science, NYUAD Institute, New York University Abu Dhabi, Abu Dhabi, UAE

⁵ LIRA, Observatoire de Paris, Université PSL, Sorbonne Université, Université Paris Cité, CY Cergy Paris Université, CNRS, 92190 Meudon, France

Received ⟨date⟩ / Accepted ⟨date⟩

ABSTRACT

Aims. We study the temporal evolution of solar inertial modes over the solar cycle using observations from GONG and SDO/HMI. We focus our attention on the high-latitude mode with azimuthal wavenumber $m = 1$ and the equatorial Rossby modes with $3 \leq m \leq 16$.

Methods. We use maps of horizontal flows near the solar surface from the GONG and HMI (p-mode) ring-diagram pipelines at a cadence of approximately one day, covering the period 2002–2024. The data are divided into overlapping four-year windows, with central times separated by six months. Within each time window and for each inertial mode, we measure the frequency and the power of the mode from the GONG and the HMI data.

Results. We find good agreement between the GONG and HMI measurements throughout their overlapping period from 2010 to 2024. In general, the magnitude of the frequency variations increases with increasing m , while relative changes in mode power typically exceed 100%. For the $m = 1$ high-latitude mode, the measured power is anti-correlated with the sunspot number, while its frequency shows no significant temporal variation. For the equatorial Rossby modes, the frequencies are generally anti-correlated with the sunspot number, whereas the mode powers tend to correlate positively with the sunspot number. An exception is the $m = 3$ equatorial Rossby mode, whose mode power is strongly anti-correlated with the sunspot number, in contrast to the other equatorial Rossby modes, highlighting its distinct behavior.

Conclusions. We find that the frequencies and power of the Sun’s inertial modes exhibit significant variability on solar-cycle timescales over the past 23 years. The mode parameters are however not uniformly synchronized with the sunspot number; clear differences are observed both from mode to mode and from one solar cycle to the next. The sensitivity of inertial modes to solar-cycle changes indicates their potential as a diagnostic of solar interior dynamics and magnetism.

Key words. Sun: rotation – Sun: oscillations – Sun: solar cycle – Sun: helioseismology

1. Introduction

Equatorial Rossby (ER) modes on the Sun, also referred to as sectoral Rossby modes, were first identified observationally by Löptien et al. (2018) for longitudinal wavenumbers $3 \leq m \leq 15$. Subsequent work by Gizon et al. (2021) and Hanson et al. (2022) revealed additional families of inertial modes with maximum vorticity amplitudes peaking at mid and high latitudes. The high-latitude (HL) modes occur for $1 \leq m \leq 5$, with the $m = 1$ mode dominating in amplitude (~ 10 m/s) and peaking above 60° latitude. A recent overview of solar inertial modes is given by Gizon et al. (2024) and references therein.

The parameters of the Sun’s inertial modes vary over the solar cycle. For the ER modes, Waidele & Zhao (2023) showed that the average power of modes with $3 \leq m \leq 16$ is enhanced in HMI helioseismic flow maps during the maximum of solar cycle 24 (around 2014) and reduced during the solar minimum between cycles 24 and 25, while the average mode frequency decreases during solar maximum. In contrast, the $m = 1$ HL

mode exhibits an opposite amplitude trend: using direct Doppler observations (combining HMI, GONG, and WSO) covering the last five solar cycles, Liang & Gizon (2025) found that the mode power is anti-correlated with the solar cycle, whereas the mode frequency shows only weak variations and no clear cycle dependence.

As noted by Gizon et al. (2021) and Bekki et al. (2022a), numerical models indicate that solar inertial modes are sensitive to conditions throughout much of the convection zone. The solar-cycle variations observed in their frequencies are therefore likely caused by a combination of perturbations in the solar interior. The most prominent candidates are changes in the solar differential rotation Goddard et al. (2020) and variations in the global solar magnetic field (Mukhopadhyay & Gizon 2026, submitted). The stochastic excitation of the modes (Philidet & Gizon 2023) may also be affected indirectly by the magnetic field. By isolating and removing the effects associated with the well-understood changes in the differential rotation (e.g., Vorontsov et al. 2002; Howe 2009), measurements of the solar-cycle variations of the inertial modes offer the exciting prospect of placing meaningful

* Corresponding author: gizon@mps.mpg.de

constraints on the Sun’s global magnetic field in the bulk of the convection zone. This prospect provides a strong motivation for detailed studies of inertial-mode variability.

In this paper, we further characterize the parameters of solar inertial modes using ring-diagram flow maps spanning the GONG (2001–2024) and HMI (2010–2024) observing periods. By comparing these two independent data sets, we aim to confirm the reported frequency variations. In addition, we present time-dependent parameters for individual modes, rather than averages over mode sets.

2. Observations

2.1. Overview of the datasets

We utilize near-surface zonal and meridional flow measurements derived from the ring-diagram (RD) pipelines of GONG (Hill et al. 2003; Corbard et al. 2003) and HMI (Bogart et al. 2011a,b), spanning January 2002 to September 2024 and July 2010 to September 2024, respectively. The RD pipeline provides flow measurements by analyzing shifts in p-mode frequencies obtained from tracked patches of Doppler velocity measurements (Haber et al. 2002).

In the GONG RD pipeline, full-disk Dopplergrams from multiple GONG sites are merged and remapped into overlapping patches of size $15^\circ \times 15^\circ$, with centers separated by 7.5° . These patches cover latitudes and central meridian distances (CMD) within $\pm 52.5^\circ$. For this study, flows at four additional latitudes, $\pm 60^\circ$ and $\pm 67.5^\circ$, are also included. Each patch is tracked for 1664 minutes at the Snodgrass rotation rate (Snodgrass 1984).

The HMI RD pipeline uses overlapping patches of the same size, tracked at the sidereal Carrington rotation rate. These patches cover latitudes and CMDs within $\pm 75^\circ$. The latitudinal spacing is identical to that of GONG, while the CMD separation is 7.5° within $\pm 30^\circ$ latitude and becomes coarser at higher latitudes. To ensure consistency, we interpolate the HMI flows in CMD (Proxauf et al. 2020) to match the GONG grid points, covering latitudes from -67.5° to 67.5° .

2.2. Post-processing of ring-diagram data

The temporal cadence of GONG and HMI flow maps is, on average, about 27.2753 hours. To remove the annual and zero-frequency components from the GONG and HMI measurements, we fit the time series with sinusoids and subtract the resulting fits from the flow maps in the Stonyhurst frame (Proxauf et al. 2020).

Since the GONG RD pipeline utilizes ground-based daily observations from different sites, an additional one-day periodicity is introduced into the data. The frequency corresponding to this one-day period is $11.6 \mu\text{Hz}$. Due to aliasing, this frequency appears at $1.4 \mu\text{Hz}$, as the Nyquist frequency for our dataset is $5.1 \mu\text{Hz}$. This aliased frequency corresponds to a periodicity of approximately 8.33 days. We also remove this additional periodicity from the GONG data.

The zonal and meridional flows in the Stonyhurst frame are transformed into the Carrington frame to obtain $u_\phi(\theta, \phi, t)$ in the longitudinal direction and $u_\theta(\theta, \phi, t)$ in the co-latitudinal direction at the observation time t . The Carrington longitude (ϕ) increases in the prograde direction, and the co-latitude (θ) increases southward.

3. Measurements of mode parameters

3.1. Mode parameters from mean spectra

We divide the observation periods of GONG and HMI into overlapping time segments of size $T = 4$ years, with the centers shifted by multiples of six months. The central times of the GONG segments are given by $t_n = 1 \text{ Jan 2004} + n \times 6 \text{ months}$, where n ranges from 0 to 38, covering the period from 2002 to 2024. For HMI, the central times are $t_n = 1 \text{ Jul 2012} + n \times 6 \text{ months}$, with n ranging from 0 to 21, covering the period from mid 2010 to 2024.

The flow maps within each time segment are symmetrized (+) or anti-symmetrized (−) with respect to the equator, to obtain $u_j^s(\theta, \phi, t)$, where s represents the symmetry and j represents either θ or ϕ . The ER modes are stronger in the u_θ^+ component, while the $m = 1$ HL mode is stronger in u_ϕ^- . Therefore, we utilize these components to compute their respective power spectral density:

$$P_j^s(\theta, m, \nu, t_n) = \eta_1 \eta_2 \left| \sum_{\phi, t'} \text{rect}\left(\frac{t' - t_n}{T}\right) u_j^s(\theta, \phi, t') e^{i(m\phi - 2\pi\nu t')} \right|^2, \quad (1)$$

where the function “rect” refers to a rectangular window, defined by $\text{rect}(\xi)$ equals to 1 for $|\xi| < 1/2$ and zero otherwise. The azimuthal wavenumber m is taken to be a positive integer throughout this paper. The temporal frequency ν is measured in the Carrington frame (retrograde propagation occurs at $\nu < 0$). The factor $\eta_1 = N_\phi^2 N_t^2 / (N_\phi'^2 N_t'^2)$ corrects for the reduction in power due to missing data in time and partial coverage in longitude. Here, N_ϕ and N_t represent the total number of grid points in longitude and time within each time segment, while N_ϕ' and N_t' denote the number of available data points. The factor $\eta_2 = 2 / (\text{d}\nu N_\phi^2 N_t^2)$ is a normalisation factor, where $\text{d}\nu = 8 \text{ nHz}$ is the frequency resolution. With this definition, the power P_m has units of $\text{m}^2 \text{s}^{-2} \text{ nHz}^{-1}$.

For studying the ER modes we average P_θ^+ over latitude bins within $\pm 30^\circ$ around the equator, while for the HL mode, we use P_ϕ^- only at the highest latitude bin 67.5° . That is,

$$P_m(\nu, t_n) = \begin{cases} P_\phi^-(\theta = 22.5^\circ, m, \nu, t_n) & \text{for HL mode,} \\ \langle P_\theta^+(\theta, m, \nu, t_n) \rangle_{|90^\circ - \theta| \leq 30^\circ} & \text{for ER modes.} \end{cases} \quad (2)$$

We compute a reference power spectrum, $\bar{P}_m(\nu)$, for each m by averaging P_m from GONG over five non-overlapping time segments covering 2002–2021. The peak of power associated with each mode in the respective mean power spectrum is fitted with a Lorentzian profile,

$$L_m(\nu) = \bar{A}_m \left[1 + \left(\frac{\nu - \bar{\nu}_m}{\bar{\Gamma}_m/2} \right)^2 \right]^{-1} + \bar{B}_m, \quad (3)$$

where \bar{A}_m , $\bar{\nu}_m$, $\bar{\Gamma}_m$, and \bar{B}_m represent the Lorentzian’s height, central frequency, full width at half maximum, and a constant background, respectively. For each mode, it is important to choose a fitting range that excludes spatial leakage from neighboring m ’s as well as low-frequency power from active-region flows. Table A.1 lists the fitting range for each mode. The larger fitting range for higher m modes accounts for the larger mode linewidths. The mode parameters are estimated from the data using the maximum likelihood method (see Appendix B).

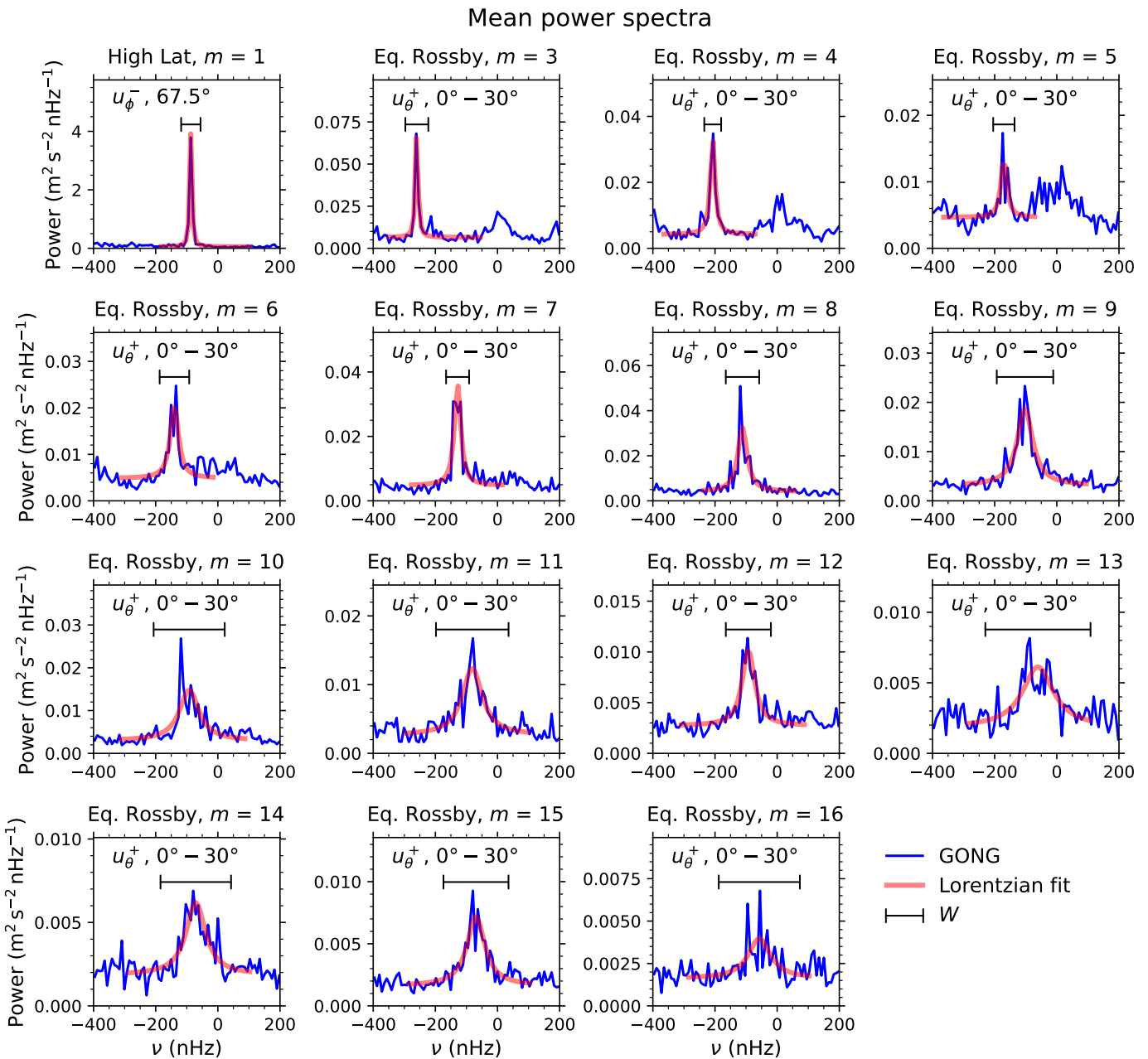


Fig. 1: GONG reference power spectra $\bar{P}_m(\nu)$ (blue curves) with frequency resolution $d\nu = 8$ nHz. The top left panel shows $\bar{P}_m(\nu)$ for the $m = 1$ component of u_ϕ^- ; the peak corresponds to the $m = 1$ high-latitude mode. All other panels show $\bar{P}_m(\nu)$ for the u_θ^+ component of the flow and different m values ranging from 3 to 16. The red curves show the Lorentzian fits to the power spectra (Sect. 3.1). The horizontal black segments show the frequency windows W used to extract the mode parameters from consecutive 4-year power spectra (see Sect. 3.2).

We define the 'mode power' in the mean power spectrum as the product of the height and width of the Lorentzian,

$$\bar{E}_m = \bar{A}_m \times \bar{\Gamma}_m. \quad (4)$$

We note, however, that the integrated power of the mode above the background level, i.e. the area under the Lorentzian profile, is given by $(\pi/2) \bar{A}_m \bar{\Gamma}_m$. The physically meaningful mode power therefore differs from \bar{E}_m by a factor of $\pi/2$. For simplicity, and with a slight abuse of terminology, we will nevertheless refer to \bar{E}_m as the mode power throughout the remainder of this paper.

Table 1 provides the mode parameters and Fig. 1 shows the mean GONG spectra, $\bar{P}_m(\nu)$, along with the Lorentzian fits for $m = 1$ HL and $3 \leq m \leq 16$ ER modes. A comparison between the mean GONG and HMI spectra for the period 2010.5–2022.5 is shown in Fig. C.1, demonstrating that the two datasets are consistent with each other.

The measured mean mode powers are plotted in Fig. 2 for all modes of interest. The Rossby modes have powers in the range 0.2 – $1.0 \text{ m}^2/\text{s}^2$. A comparison is provided in Fig. 2 between the measured mode powers and the model of Philedit & Gizon (2023); this 2D model in the β -plane is based on the stochastic

Table 1: Mode parameters measured from the reference GONG power spectra (2002–2021).

m	(j, s)	\bar{v}_m (nHz)	$\bar{\Gamma}_m$ (nHz)	\bar{E}_m ($\text{m}^2 \text{s}^{-2}$)	SNR
<i>High-latitude mode</i>					
1	$(\phi, -)$	$-86.9^{+1.4}_{-1.4}$	$7.8^{+2.6}_{-2.4}$	$30.2^{+9.08}_{-7.00}$	$73.6^{+54.9}_{-28.4}$
<i>Equatorial Rossby modes</i>					
3	$(\theta, +)$	$-259.6^{+1.1}_{-1.2}$	$9.2^{+2.4}_{-2.8}$	$0.6^{+0.14}_{-0.10}$	$10.3^{+5.8}_{-2.8}$
4	$(\theta, +)$	$-207.4^{+1.6}_{-1.6}$	$18.1^{+4.3}_{-3.9}$	$0.5^{+0.08}_{-0.07}$	$6.9^{+2.1}_{-1.5}$
5	$(\theta, +)$	$-170.4^{+3.2}_{-3.1}$	$22.9^{+9.5}_{-8.8}$	$0.2^{+0.06}_{-0.05}$	$1.9^{+0.9}_{-0.5}$
6	$(\theta, +)$	$-139.7^{+2.8}_{-2.8}$	$31.7^{+8.5}_{-7.9}$	$0.5^{+0.09}_{-0.08}$	$3.2^{+1.0}_{-0.6}$
7	$(\theta, +)$	$-128.4^{+1.9}_{-1.9}$	$24.7^{+5.3}_{-4.8}$	$0.8^{+0.10}_{-0.10}$	$6.7^{+1.7}_{-1.3}$
8	$(\theta, +)$	$-111.6^{+2.3}_{-2.2}$	$35.8^{+6.6}_{-6.2}$	$1.0^{+0.13}_{-0.12}$	$7.0^{+1.6}_{-1.1}$
9	$(\theta, +)$	$-102.4^{+3.3}_{-3.2}$	$60.6^{+10.7}_{-10.1}$	$0.9^{+0.12}_{-0.10}$	$5.0^{+1.0}_{-0.7}$
10	$(\theta, +)$	$-92.3^{+3.9}_{-4.1}$	$76.2^{+15.0}_{-13.2}$	$0.9^{+0.13}_{-0.11}$	$4.0^{+0.8}_{-0.5}$
11	$(\theta, +)$	$-81.3^{+4.1}_{-4.1}$	$77.8^{+15.3}_{-14.2}$	$0.8^{+0.12}_{-0.10}$	$3.7^{+0.8}_{-0.5}$
12	$(\theta, +)$	$-92.7^{+3.7}_{-3.8}$	$48.4^{+11.9}_{-10.8}$	$0.4^{+0.06}_{-0.06}$	$2.8^{+0.7}_{-0.5}$
13	$(\theta, +)$	$-60.8^{+6.3}_{-6.5}$	$120.9^{+32.2}_{-28.2}$	$0.5^{+0.14}_{-0.11}$	$2.4^{+0.7}_{-0.4}$
14	$(\theta, +)$	$-71.0^{+5.1}_{-4.9}$	$75.7^{+19.3}_{-17.3}$	$0.3^{+0.07}_{-0.06}$	$2.3^{+0.6}_{-0.3}$
15	$(\theta, +)$	$-69.3^{+4.0}_{-4.0}$	$69.7^{+14.1}_{-13.3}$	$0.4^{+0.06}_{-0.05}$	$3.5^{+0.7}_{-0.5}$
16	$(\theta, +)$	$-57.5^{+6.9}_{-7.1}$	$87.0^{+29.6}_{-25.5}$	$0.2^{+0.07}_{-0.05}$	$1.5^{+0.4}_{-0.2}$

Notes. Frequencies (\bar{v}_m), linewidths ($\bar{\Gamma}_m$), mode powers ($\bar{E}_m = \bar{A}_m \times \bar{\Gamma}_m$), and signal-to-noise ratios (SNR = \bar{A}_m / \bar{B}_m) for each mode. The corresponding flow component and symmetry used to compute $\bar{P}_m(v)$ are denoted by $j = \theta, \phi$ and $s = +, -$, respectively. The upper and lower bounds indicate the 68% confidence levels of the parameters obtained from Monte Carlo simulations.

excitation of purely toroidal modes by turbulent convection. The agreement between observations and model is reasonable. The power of the $m = 1$ HL mode stands out at $30.2 \text{ m}^2/\text{s}^2$ in the average GONG spectrum. This value may be related to the HMI maximum velocity amplitude of 9.8 m s^{-1} above 67.5° reported by Gizon et al. (2021). In the present work the highest latitude bin available is only 67.5° , corresponding to a lower amplitude of 5.5 m s^{-1} .

The solar $m = 1$ HL mode is self-excited by a baroclinic instability (Bekki et al. 2024), thus explaining why it reaches such a high amplitude in the Sun. However, all the other modes discussed here are linearly stable, and their excitation is due instead to the highly turbulent motions characterising the solar convective zone, in a manner similar to the stochastic excitation of the solar p-modes (Philidet & Gizon 2023).

3.2. Mode parameters from individual time segments

We measure the mode frequencies and powers in individual 4-year time segments to study their temporal variations. Because some modes are not significant in certain periods, the Lorentzian fit may not perform well. We therefore develop a more robust approach for determining the mode parameters.

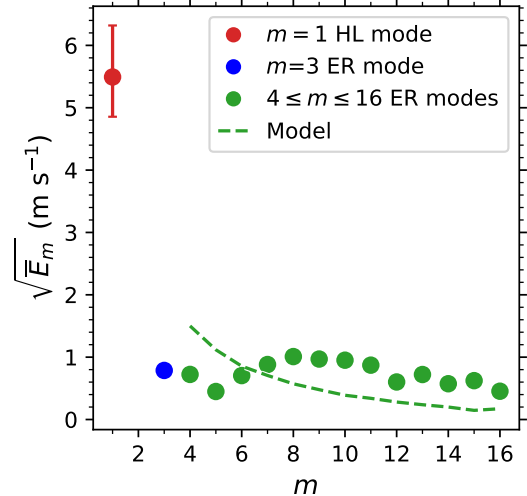


Fig. 2: Square root of mode power as a function of m for the GONG observations (\bar{E}_m from Table 1). The stochastic excitation model from Philidet & Gizon (2023) is overplotted.

We define the mode frequency (v_m) and the mode power (E_m) in each time segment (t_n) as

$$v_m(t_n) = \frac{\sum_{v \in W} v \times P_m(v, t_n)}{\sum_{v \in W} P_m(v, t_n)}, \quad (5)$$

$$E_m(t_n) = \frac{dv}{\arctan(w/\bar{\Gamma}_m)} \sum_{v \in W} [P_m(v, t_n) - B_m(t_n)], \quad (6)$$

where W is the frequency window over which the sums are computed (see Table A.1, right column), and w is the width of the frequency window. The window W , centered at the mean frequency \bar{v}_m and with a width of at least $2\bar{\Gamma}_m$, is selected to encompass the majority of the mode power. The normalization factor $\arctan(w/\bar{\Gamma}_m)$ is introduced so that E_m can be directly compared to the product $A_m \bar{\Gamma}_m$ (correction for the missing power in the wings of the Lorentzian beyond the interval W). The background power $B_m(t_n)$ depends on the phase of the solar cycle and is estimated by computing the median power just outside of the window W .

The values of v_m and E_m are shown in Figs. 3 and 4. The parameters obtained from GONG and HMI are consistent during their overlap period (2010–2024). Furthermore, the mode powers and frequencies exhibit significant temporal variations in most cases. Figure 4 also shows the background power variations. It is evident that the mode power variations are not caused by changes in the background power. The background power of GONG is higher than that of HMI, likely due to a larger number of missing data points.

We estimate the uncertainties in v_m and E_m using Monte Carlo simulations. We generate 10 000 realisations of a model spectrum with linewidth $\Gamma_m = \bar{\Gamma}_m$, amplitude $A_m = E_m / \bar{\Gamma}_m$, frequency v_m , and background B_m . The 68% confidence intervals of the resulting parameter distributions are taken as the uncertainty bounds for the v_m and E_m .

For a subset of modes, Lorentzian fits performed on four-year time segments are robust. These include the $m = 1$ high-latitude mode, and the $m = 4, 8, 12$, and 14 Rossby modes. For these 5 modes, we are able to extract reliable temporal variations of the mode linewidths Γ_m , in the sense that the product of

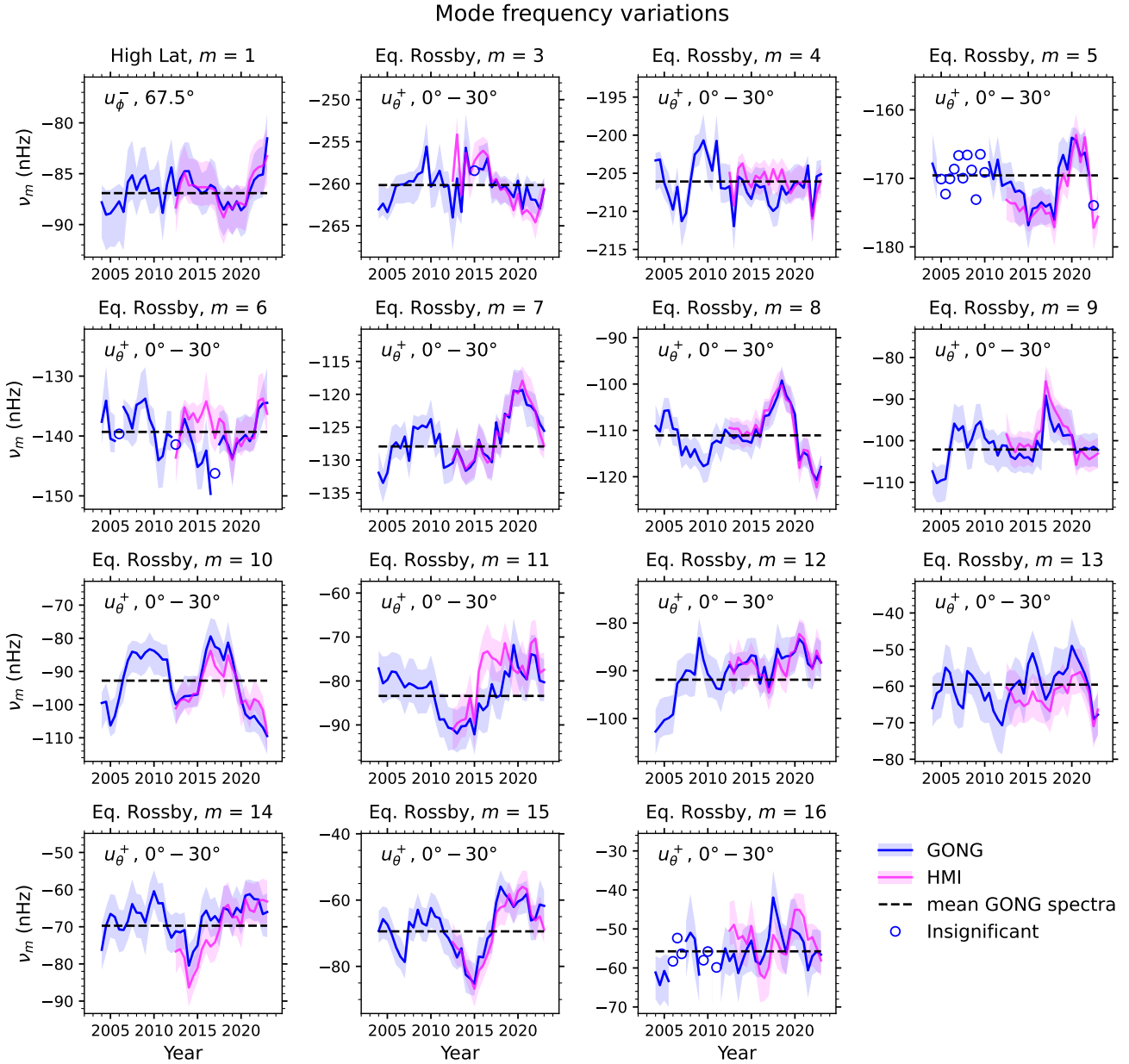


Fig. 3: Temporal variations of the mode frequencies (v_m) obtained from the GONG (blue) and HMI (magenta) datasets. The top left panel is for the $m = 1$ high-latitude mode, the other panels for the equatorial Rossby modes. The shaded regions indicate the 68% confidence intervals of v_m estimated from Monte Carlo simulations. Mode frequencies shown as open circles indicate no significant power (< 95% confidence) in the corresponding time segments. The mode frequencies obtained from the reference GONG data (2002–2021) are shown as horizontal dashed lines.

the fitted Lorentzian amplitude and line width is consistent with the independently measured mode power E_m obtained using the method described above. The results are shown in Appendix C.2. For the remaining modes, the Lorentzian fits are not sufficiently stable across the four-year segments, and the resulting parameters do not show satisfactory consistency with the corresponding mode power E_m . We therefore do not consider these fits reliable and do not report these modes from the analysis based on Lorentzian fitting.

3.3. Comparison of power spectra from Fourier and wavelet analyses

The top panels of Fig. 5 show the latitudinally averaged Fourier power, $P_m(v, t_n)$, for each 4-year time segment of the $m = 1$ HL mode and the $m = 3$ and $m = 9$ ER modes, as a function of time and frequency. The frequencies $v_m(t_n)$, calculated using Eq. (5), are plotted over the Fourier spectra for comparison. The measured v_m closely follow the excess power within the frequency window W . The time periods during which the excess power peaks agree well with those shown in Fig. 4.

We also perform a continuous wavelet transform using a Morlet wavelet. The bottom panels of Fig. 5 show the wavelet power of the selected modes within the inertial frequency ranges.

Mode power variations

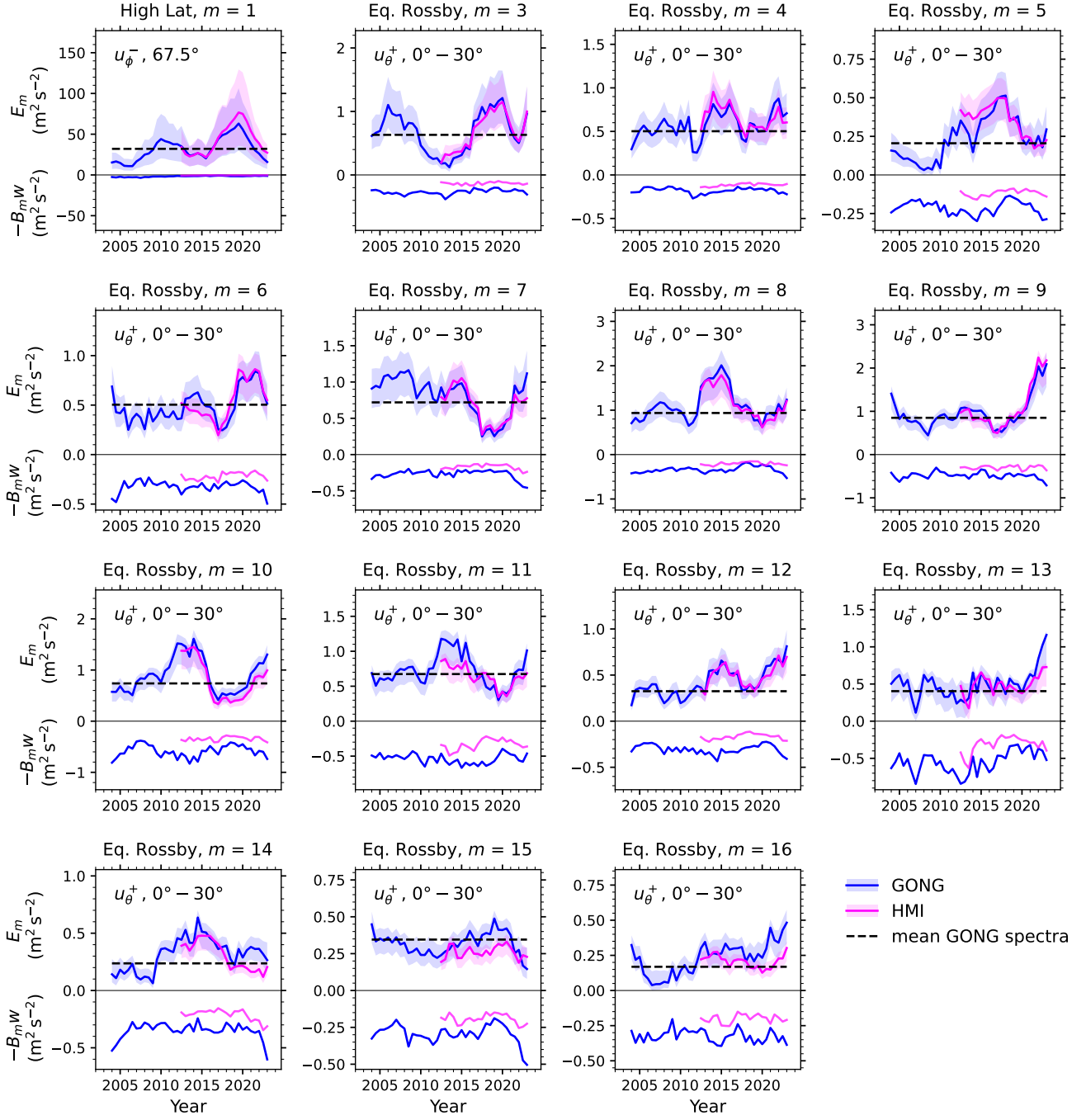


Fig. 4: Temporal variations of the mode power (E_m) and the negative of the background power ($-B_{mW}$). The top left panel is for the $m = 1$ high-latitude mode, the other panels for the equatorial Rossby modes. The powers computed from the GONG and HMI datasets are shown in blue and magenta, respectively. The shaded regions represent the 68% confidence intervals of E_m estimated from Monte Carlo simulations. The horizontal dashed lines indicate the mode powers obtained from the reference GONG data (2002–2021).

The wavelet spectra are consistent with the Fourier spectra, though they appear more smeared. The Fourier and wavelet spectra for all remaining modes are shown in Fig. C.3.

4. Temporal variations of mode parameters

4.1. Peak-to-peak variations of mode parameters

We first examine the peak-to-peak variations, i.e. the difference between the maximum and minimum values, of the mode parameters across the full GONG time series 2002–2024. The peak-to-peak variation in mode power is denoted by $\mathcal{D}E_m$, and the

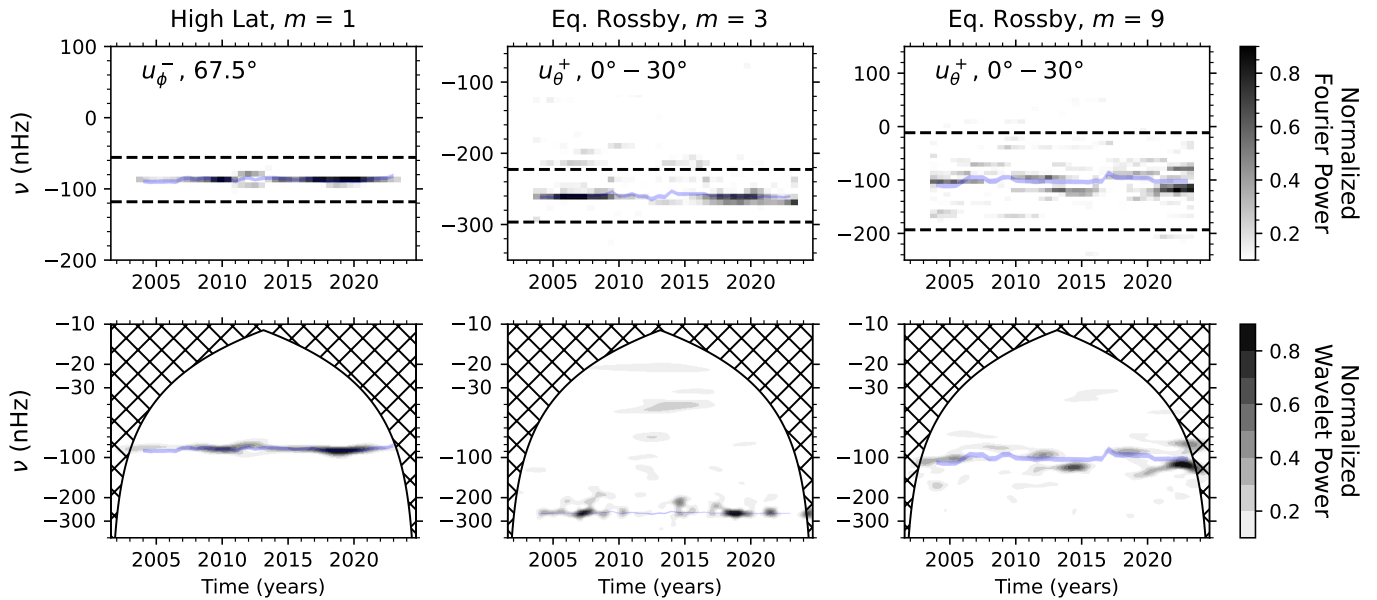


Fig. 5: Fourier (top panels) and wavelet (bottom panels) power spectra of the $m = 1$ HL and $m = 3$ and 9 ER modes, as a function of time and frequency. The frequencies $\nu_m(t_n)$, calculated using Eq. (5), are overplotted as light blue curves with widths representing the 68% confidence intervals. In the top panels, the horizontal dashed lines indicate the frequency window W used in Eqs. (5) and (6).

peak-to-peak variation in mode frequency by $\mathcal{D}\nu_m$. The values of $\mathcal{D}E_m$ exceed 100% for all modes, as can be seen in Fig. 6a. Most values of $\mathcal{D}E_m$ are between 100% and 200%, while the Rossby modes $m = 5, 13, 14, 16$ are above 200%. Although the $m = 1$ HL mode has a power that is two orders of magnitude larger than ER modes (see Table 1), its relative peak-to-peak variation is of the same order as that of the ER modes.

Figure 6b shows the peak-to-peak variations $\mathcal{D}\nu_m$. The least significant $\mathcal{D}\nu_m$ is for the $m = 1$ high-latitude mode. In all other cases $\mathcal{D}\nu_m$ is above three times its associated error. The values of $\mathcal{D}\nu_m$ increase with increasing m up to $m \approx 8$; for $m \gtrsim 8$, there seems to be a plateau around $\mathcal{D}\nu_m \approx 25$ nHz. For low m values, the peak-to-peak variations in ν correspond to less than about 10% of their mean frequencies in the corotating frame, which is much smaller than the relative mode power variations.

4.2. Correlations with sunspot number

We calculated the Pearson correlation coefficients between the time series of mode parameters and the sunspot number (SSN). The SSN data, obtained from the World Data Center SILSO, Royal Observatory of Belgium (Clette & Lefèvre 2015), are averaged over 4-year time segments, for comparison with our data. The correlation coefficients are listed in Table 2 for the full GONG period (2002–2024) and for the HMI-GONG overlap period (2010–2024).

Figure 6c shows the correlation coefficients between the mode powers and the SSN over the full GONG period for each m . The mode power of the $m = 1$ HL mode has an anti-correlation of -0.5 with the SSN. We note that Liang & Gizon (2025) also report a correlation of -0.5 based on observations spanning five solar cycles. The $m = 3$ ER mode stands out in Fig. 6c, exhibiting the strongest anti-correlation of -0.7 , in contrast to the positive correlation coefficients of most other ER modes. We therefore highlight the $m = 3$ ER mode with a different color in this plot.

Table 2: Pearson correlation coefficients between the SSN and mode parameters obtained from the GONG dataset for the full GONG period 2002–2024 and for the GONG period that overlaps with HMI (2010–2024).

m	GONG 2002–2024		GONG 2010–2024	
	Correlations		Correlations	
	(E, SSN)	(ν, SSN)	(E, SSN)	(ν, SSN)
<i>High-latitude mode</i>				
1	-0.50	0.38	-0.91	0.78
<i>Equatorial Rossby modes</i>				
3	-0.70	-0.21	-0.83	0.07
4	0.16	-0.02	0.43	0.10
5	0.15	-0.37	-0.34	-0.46
6	0.24	-0.00	0.04	0.31
7	0.34	-0.60	0.91	-0.66
8	0.50	-0.20	0.78	-0.61
9	0.53	-0.60	0.43	-0.61
10	0.65	-0.55	0.90	-0.45
11	0.72	-0.52	0.92	-0.67
12	0.38	-0.27	0.41	-0.32
13	0.20	-0.37	0.20	-0.50
14	0.45	-0.58	0.54	-0.59
15	-0.39	-0.53	-0.76	-0.71
16	0.51	-0.50	0.36	-0.63

Figure 6d shows the correlation coefficients between the mode frequencies and the SSN. In general, the ER-mode frequencies are anti-correlated with the SSN. For $m \gtrsim 8$, the correlations mostly fall between -0.4 and -0.6 , whereas at smaller m they are more scattered, with values between 0 and -0.6 . The

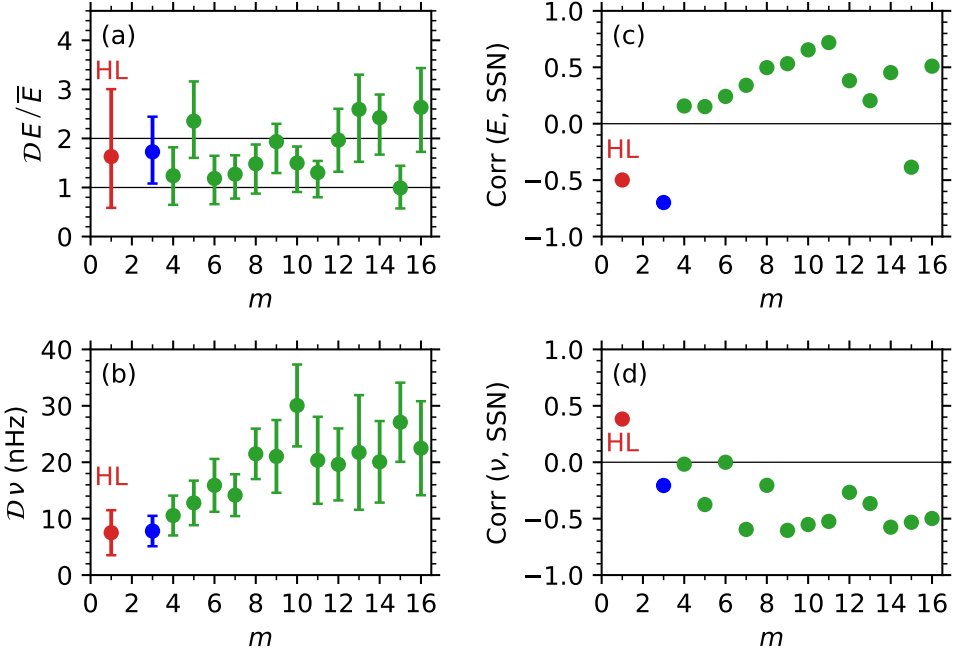


Fig. 6: Solar cycle variability of mode parameters. (a) Relative peak-to-peak variation of mode powers over the GONG period 2002–2024. Error bars indicate the 68% confidence intervals. (b) Peak-to-peak variation of mode frequencies over the GONG period 2002–2024. (c) Correlation coefficients between the time series of mode powers and the sunspot numbers, computed over the full GONG period. (d) Same as panel (c), but for mode frequencies. The values for the $m = 1$ high-latitude mode are shown in red, those for the $m \geq 4$ Rossby modes in green. The $m = 3$ Rossby mode is shown in blue.

$m = 3$ mode shows a negative correlation of -0.2 with the SSN. Although the $m = 1$ HL mode shows a positive correlation of 0.4 , the frequency variations are almost always within the uncertainties (see the top left panel of Fig. 3) and should not be overinterpreted.

4.3. Mode power variations

Since the powers of most of the ER modes (except the $m = 3$) show a positive correlation with the SSN over the full GONG period, we study these modes together. To investigate whether there are common patterns, we stack the time series of the mode powers over m . The middle panel of Fig. 7 shows the temporal variations in the normalized mode power, E_m/\bar{E}_m , for $4 \leq m \leq 16$ ER modes. Although they are positively correlated with the SSN, they do not peak exactly at the solar maximum. The modes with $9 \leq m \leq 11$ peak around the solar maximum, slightly toward the rising phase, whereas modes with lower and higher m tend to peak during the declining phase.

Panels a and b of Fig. 8 compare the normalized power for the $m = 1$ HL mode, the $m = 3$ and $m = 10$ ER modes, and the average over $4 \leq m \leq 16$ for the ER modes. The averaged power is defined as

$$\langle E/\bar{E} \rangle = \sum_{m=4}^{16} \alpha_m(t) \frac{E_m(t)}{\bar{E}_m}, \quad \alpha_m := \frac{1/\sigma_{E_m}^2}{\sum_{m'} 1/\sigma_{E_{m'}}^2}, \quad (7)$$

where σ_{E_m} is the uncertainty in E_m , normalized by \bar{E}_m .

Although the $m = 1$ HL and $m = 3$ ER mode powers are both anti-correlated with the SSN over the full GONG period, their E_m/\bar{E}_m time series show patterns similar to those of the $4 \leq m \leq 16$ ER modes, in that the power does not peak exactly at

the phase implied by the correlation. Both modes peak near the cycle 24/25 minimum, but their peak power is offset from the cycle 23/24 minimum earlier in the time series. This temporal offset weakens the overall anti-correlations compared with those obtained during the HMI-GONG overlap period, suggesting that the timing of peak power varies from cycle to cycle.

As a representative example of the $4 \leq m \leq 16$ range, the $m = 10$ ER mode shows a temporal evolution similar to that of the ER-set, but its peak power occurs closer to the rising phase of the solar cycle. Meanwhile, the averaged power, $\langle E/\bar{E} \rangle$, over $4 \leq m \leq 16$ shows a strong correlation with the SSN, with coefficients of 0.77 for the full GONG period (2002–2024) and 0.89 for the HMI-GONG overlap period (2010–2024). The lower correlation over the longer time interval reflects the impact of cycle-to-cycle phase shifts.

During the solar activity cycle, strong magnetic fields may inhibit convection, thus affecting the efficiency with which turbulence in the convective zone drives the inertial modes, and directly impacting their excitation rate. At the same time, the turbulent viscosity, being tightly related to the convective turbulent spectrum, is also likely to have a solar-cycle dependence. Because the Rossby mode power is the result of a balance between driving and damping processes (that is to say, the ratio between its excitation rate and damping rate, as illustrated by Eq. (4)), its observed dependence on the solar-cycle is a valuable signature of how the convection, alongside the internal magnetic field and the torsional oscillation, evolves along the activity cycle. In this context, numerical simulations constitute a very useful tool to investigate the behaviour of inertial modes, and in particular the degree to which they are excited under different physical conditions (Bekki et al. 2022b; Blume et al. 2024; Fuentes et al. 2025).

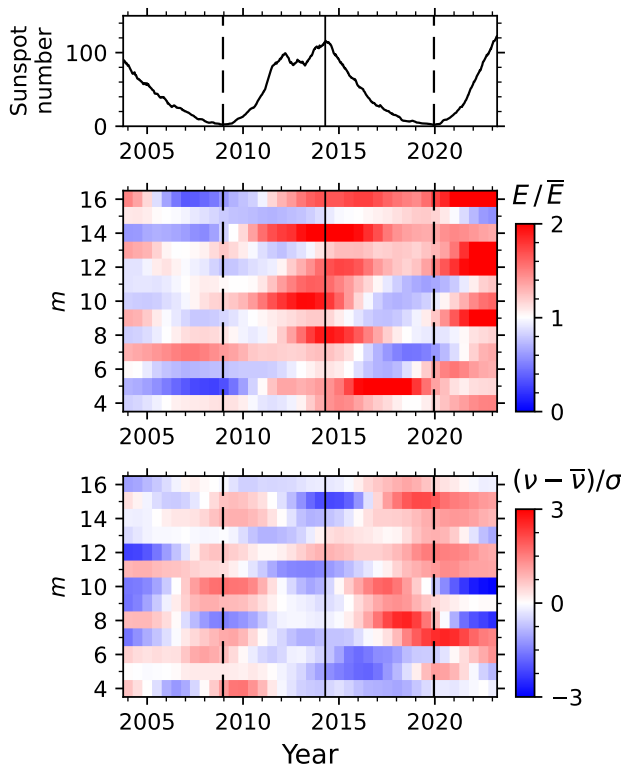


Fig. 7: Normalized Rossby mode powers (middle) and frequency shifts in units of frequency uncertainties (bottom) for $4 \leq m \leq 16$. Top panel shows the sunspot number in the corresponding time period. The GONG data are smoothed using a 3-year boxcar for clarity.

4.4. Mode frequency variations

The bottom panel of Fig. 7 shows the temporal variations of the mode frequency shifts, normalized by their respective uncertainties, $(v_m - \bar{v}_m)/\sigma_{v_m}$, for the $4 \leq m \leq 16$ ER modes, where σ_{v_m} denotes the uncertainty in v_m . Overall, the frequency shifts are anti-correlated with the SSN; however, their temporal evolution does not consistently coincide with solar minima, particularly during the latter half of the time series. While several modes exhibit positive frequency shifts near the cycle 23/24 minimum, similar enhancements occur at different phases in the subsequent cycle, indicating that the timing of the extrema is not fixed from cycle to cycle.

Panels c and d of Fig. 8 compare the normalized frequency shifts $(v_m - \bar{v}_m)/\sigma_{v_m}$ for the $m = 1$ HL mode and the $m = 3$ and $m = 10$ ER modes, together with the frequency shift averaged over $4 \leq m \leq 16$. The frequency variations of the $m = 1$ HL and $m = 3$ ER modes remain mostly within $\pm \sigma_{v_m}$ and therefore have a low signal-to-noise ratio over the full GONG period. As a representative example within the set of $4 \leq m \leq 16$ ER modes, the $m = 10$ ER mode exhibits a clearer and more coherent temporal evolution than the low- m modes. Its first positive frequency shift coincides with the cycle 23/24 minimum, consistent with the overall anti-correlation with the SSN. However, the second positive frequency shift does not occur near the subsequent minimum but instead appears during the declining phase of the solar cycle. This behavior illustrates that even for ER modes with relatively high signal-to-noise ratio, the phase of the frequency extrema can vary from one cycle to the next.

In contrast, the frequency shift averaged over $4 \leq m \leq 16$ shows a very significant variation ranging from -3 to 4 times the standard deviation of the reduced noise. The average frequency shift is strongly anti-correlated with the SSN, with correlation coefficients of -0.79 over the full GONG period (2002–2024) and -0.86 over the HMI-GONG overlap period (2010–2024). As in the case of the mode power, the reduced correlation over the longer time interval reflects cycle-to-cycle variations in the timing of the frequency extrema.

5. Conclusion

Using nearly 23 years of helioseismic flow measurements from GONG and HMI, we investigated the temporal variations in the power and frequency of the $m = 1$ high-latitude mode and the equatorial Rossby modes with $3 \leq m \leq 16$. Most modes exhibit significant temporal variability in their measured parameters, and the results obtained from the GONG and HMI data sets are consistent throughout their overlapping period (2010–2024).

For the GONG period 2002–2024, we find that the power of the $m = 1$ high-latitude (HL) mode is anti-correlated with the sunspot number (SSN), with a correlation coefficient of -0.5 (consistent with Liang & Gizon 2025). In contrast, most equatorial Rossby (ER) modes exhibit a positive correlation with the SSN, in general agreement with earlier studies (Waidele & Zhao 2023). An exception is the $m = 3$ ER mode, which shows a strong anti-correlation with the SSN (correlation coefficient -0.7), highlighting its distinctive behavior within the ER-mode family. This behavior is perhaps not unexpected, as the $m = 3$ mode lies at the intersection of the high-latitude and Rossby branches in the dispersion diagram (Gizon et al. 2021) and may therefore possess a mixed character.

For the mode frequencies during the GONG period 2002–2024, individual ER modes with $m \gtrsim 8$ show larger variations (~ 25 nHz, Fig. 6b) that are anti-correlated with the SSN (correlation coefficient around -0.5 , Fig. 6d), while modes with smaller m show weaker correlations. When the ER modes with $m \geq 4$ are considered together, the average frequency variation is highly significant at a 4σ level and it is strongly anti-correlated with the SSN (correlation coefficient -0.8 , Fig. 8d).

We further find, based on the GONG data, that the variations in mode parameters differ from one solar cycle to the next (Fig. 7). This behavior is also reflected in the correlations with the sunspot numbers: the correlation coefficients are not the same when computed over the full GONG time span (23 years) as compared to the shorter HMI period (14 years), see Table 2.

Overall, the results demonstrate that both the power and frequencies of solar inertial modes undergo substantial solar-cycle variations, but with pronounced mode-to-mode differences. The differing correlations of mode power and frequency with the sunspot number, together with the lack of strict phase coherence among modes, suggest that individual modes have different sensitivities to the underlying physical processes – differential rotation and buried magnetic fields.

Acknowledgements. The observations were acquired by GONG instruments operated by NISP/NSO/AURA/NSF with contribution from NOAA. The HMI data are courtesy of NASA/SDO and the HMI Science Team. ZCL and LG acknowledge support from ERC Synergy Grant WHOLE SUN.

References

Anderson, E. R., Duvall, Thomas L. J., & Jefferies, S. M. 1990, *ApJ*, 364, 699
 Bekki, Y., Cameron, R. H., & Gizon, L. 2022a, *A&A*, 666, A135

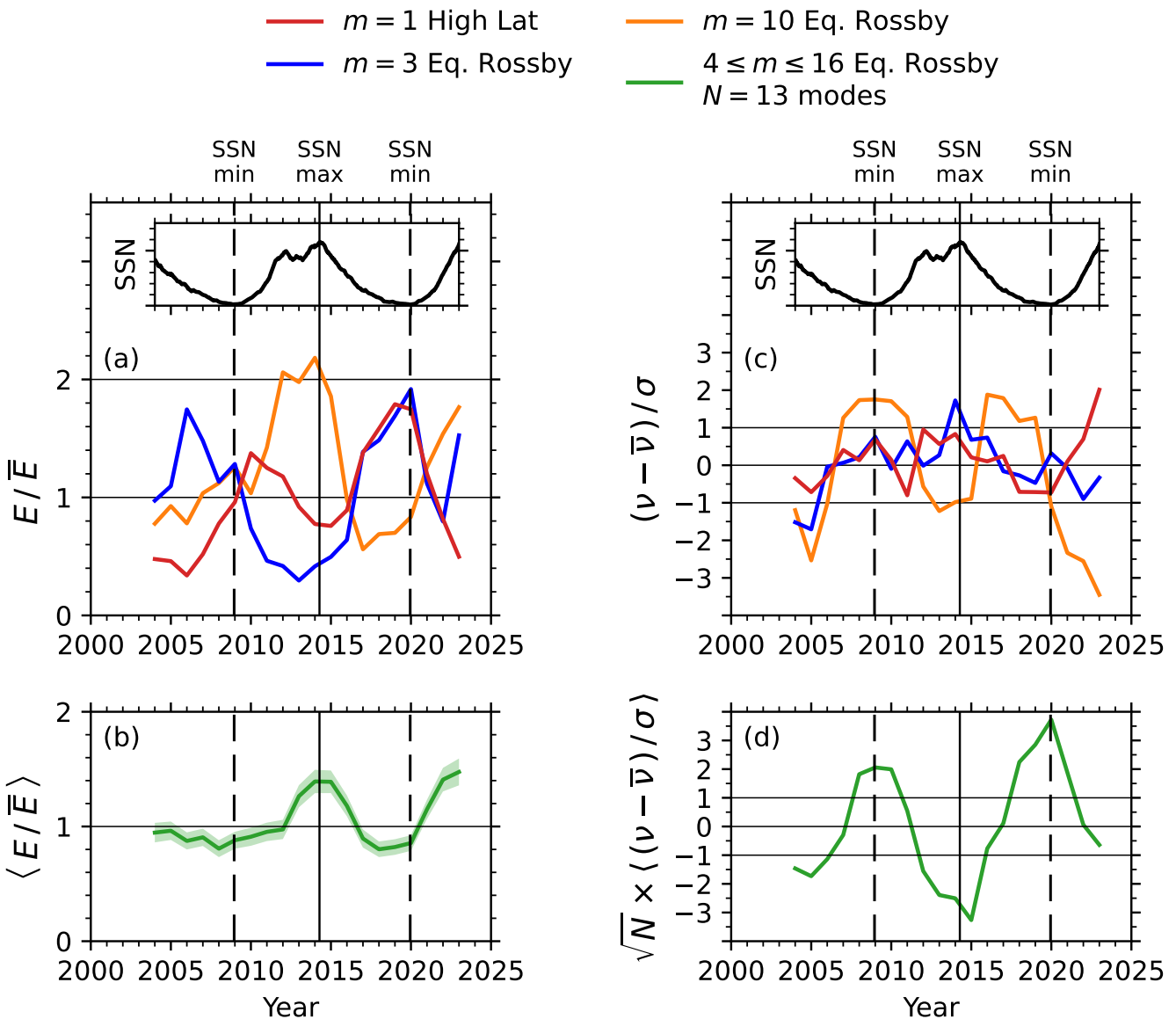


Fig. 8: Temporal variations of solar inertial mode parameters. (a) Relative mode power for three selected modes. (b) Relative mode power averaged over Rossby modes with $4 \leq m \leq 16$, see Eq. (7). (c) Mode frequency shifts divided by their uncertainties, for the same three modes as in panel (a). (d) Mode frequency shifts divided by their uncertainties averaged over $N = 13$ Rossby modes with $4 \leq m \leq 16$, and multiplied by \sqrt{N} to account for the noise reduction. In all panels, only every other data point is plotted for clarity.

Bekki, Y., Cameron, R. H., & Gizon, L. 2022b, A&A, 666, A135
 Bekki, Y., Cameron, R. H., & Gizon, L. 2024, Science Advances, 10, eadk5643
 Blume, C. C., Hindman, B. W., & Matilsky, L. I. 2024, ApJ, 966, 29
 Bogart, R. S., Baldner, C., Basu, S., Haber, D. A., & Rabello-Soares, M. C. 2011a, Journal of Physics: Conference Series, 271, 012008
 Bogart, R. S., Baldner, C., Basu, S., Haber, D. A., & Rabello-Soares, M. C. 2011b, in Journal of Physics Conference Series, Vol. 271, GONG-SoHO 24: A New Era of Seismology of the Sun and Solar-Like Stars, 012009
 Clette, F. & Lefèvre, L. 2015, SILSO Sunspot Number V2.0, <https://doi.org/10.24414/qnza-ac80>, published by WDC SILSO - Royal Observatory of Belgium (ROB)
 Corbard, T., Toner, C., Hill, F., et al. 2003, in ESA Special Publication, Vol. 517, GONG+ 2002. Local and Global Helioseismology: the Present and Future, ed. H. Sawaya-Lacoste, 255–258
 Fuentes, J. R., Barik, A., & Fuller, J. 2025, arXiv e-prints, arXiv:2511.16630
 Gizon, L., Bekki, Y., Birch, A. C., et al. 2024, in IAU Symposium, Vol. 365, IAU Symposium, ed. A. V. Getling & L. L. Kitchatinov, 207–221
 Gizon, L., Cameron, R. H., Bekki, Y., et al. 2021, A&A, 652, L6
 Goddard, C. R., Birch, A. C., Fournier, D., & Gizon, L. 2020, A&A, 640, L10
 Haber, D. A., Hindman, B. W., Toomre, J., et al. 2002, ApJ, 570, 855
 Hanson, C. S., Hanasoge, S., & Sreenivasan, K. R. 2022, Nature Astronomy, 6, 708
 Hill, F., Bolding, J., Toner, C., et al. 2003, in ESA Special Publication, Vol. 517, GONG+ 2002. Local and Global Helioseismology: the Present and Future, ed. H. Sawaya-Lacoste, 295–298
 Howe, R. 2009, Living Reviews in Solar Physics, 6, 1
 Liang, Z.-C. & Gizon, L. 2025, A&A, 695, A67
 Löptien, B., Gizon, L., Birch, A. C., et al. 2018, Nature Astronomy, 2, 568
 Mukhopadhyay, S. & Gizon, L. 2026, A&A, submitted
 Philidet, J. & Gizon, L. 2023, A&A, 673, A124
 Proxauf, B., Gizon, L., Löptien, B., et al. 2020, A&A, 634, A44
 Snodgrass, H. B. 1984, Sol. Phys., 94, 13
 Vorontsov, S. V., Christensen-Dalsgaard, J., Schou, J., Strakhov, V. N., & Thompson, M. J. 2002, Science, 296, 101
 Waidele, M. & Zhao, J. 2023, ApJ, 954, L26

Appendix A: Frequency windows for measurement of mode parameters

Table A.1: For each mode, frequency window used to fit the mean GONG power spectrum, as well as the frequency window used to measure the mode parameters in each time segment for both GONG and HMI. Frequencies are given in the Carrington frame in nHz.

m	Frequency windows [nHz, nHz]	
	mean power spectrum	4-year power spectra
<i>High-latitude mode</i>		
1	[-190, -118]	[-118, -56]
<i>Equatorial Rossby modes</i>		
3	[-350, -50]	[-297, -223]
4	[-370, -70]	[-235, -180]
5	[-370, -70]	[-205, -136]
6	[-310, -10]	[-187, -92]
7	[-280, 20]	[-165, -91]
8	[-240, 60]	[-165, -58]
9	[-300, 100]	[-193, -11]
10	[-310, 90]	[-207, 22]
11	[-300, 100]	[-198, 35]
12	[-310, 90]	[-165, -20]
13	[-290, 110]	[-230, 108]
14	[-290, 110]	[-185, 43]
15	[-290, 110]	[-174, 35]
16	[-290, 110]	[-188, 73]

Appendix B: Fitting the power spectrum averaged over multiple realisations

Appendix B.1: Statistics of the average power spectrum

At fixed frequency ν , we consider n independent realizations of the power spectrum, P_i , with $1 \leq i \leq n = 5$. Each P_i is a realization from the sum of squares of two independent centered Gaussian random variables, $U_i^2 + V_i^2$, with $\mathbb{E}[U_i^2] = \mathbb{E}[V_i^2] = \mathcal{P}/2$. We denote by $\bar{P} = \sum_{i=1}^n P_i/n$ the average power spectrum. The random variable $X = 2n\bar{P}/\mathcal{P}$ has an expectation value equal to $2n$ and is thus described by a χ^2 with $k = 2n$ degrees of freedom with probability distribution function (pdf)

$$f_X(x) = c_k x^{k/2-1} e^{-x/2}, \quad x \geq 0, \quad (\text{B.1})$$

where c_k is a normalization constant. The pdf of \bar{P} is obtained by changing variable to $p = (\mathcal{P}/2n)x$:

$$f(p; \mathcal{P}) = \frac{2n}{\mathcal{P}} f_X\left(\frac{2np}{\mathcal{P}}\right) = c_{2n}(2n)^n \left(\frac{p^{n-1}}{\mathcal{P}^n}\right) \exp\left(-\frac{np}{\mathcal{P}}\right). \quad (\text{B.2})$$

Appendix B.2: Maximum likelihood estimation

The mode parameters are measured from the averaged power spectrum \bar{P}_j over a range of independent frequencies ν_j , with $1 \leq j \leq J$. The model for the expectation value of the power spectrum is denoted by $\mathcal{P}(\nu_j, \mathbf{q})$, where the parameters \mathbf{q} are to be determined. The likelihood is given by the joint pdf evaluated at the sample data:

$$\mathcal{L}(\mathbf{q}) = \prod_{j=1}^J f\left(\bar{P}_j; \mathcal{P}(\nu_j, \mathbf{q})\right). \quad (\text{B.3})$$

The parameters \mathbf{q} are inferred by maximizing the likelihood function evaluated at the sample data, or, equivalently, minimizing

$$\begin{aligned} -\ln \mathcal{L}(\mathbf{q}) &= n \sum_{j=1}^J \left(\ln \mathcal{P}(\nu_j, \mathbf{q}) + \frac{\bar{P}_j}{\mathcal{P}(\nu_j, \mathbf{q})} \right) \\ &+ \text{terms independent of } \mathbf{q}. \end{aligned} \quad (\text{B.4})$$

Hence the maximum likelihood parameters are

$$\mathbf{q}^* = \arg \min_{\mathbf{q}} \sum_{j=1}^J \left(\ln \mathcal{P}(\nu_j, \mathbf{q}) + \frac{\bar{P}_j}{\mathcal{P}(\nu_j, \mathbf{q})} \right). \quad (\text{B.5})$$

We conclude that the estimated parameters are obtained by fitting the averaged power spectrum *as if* it were a single realization of the power spectrum (see [Anderson et al. 1990](#)).

Appendix C: Additional figures

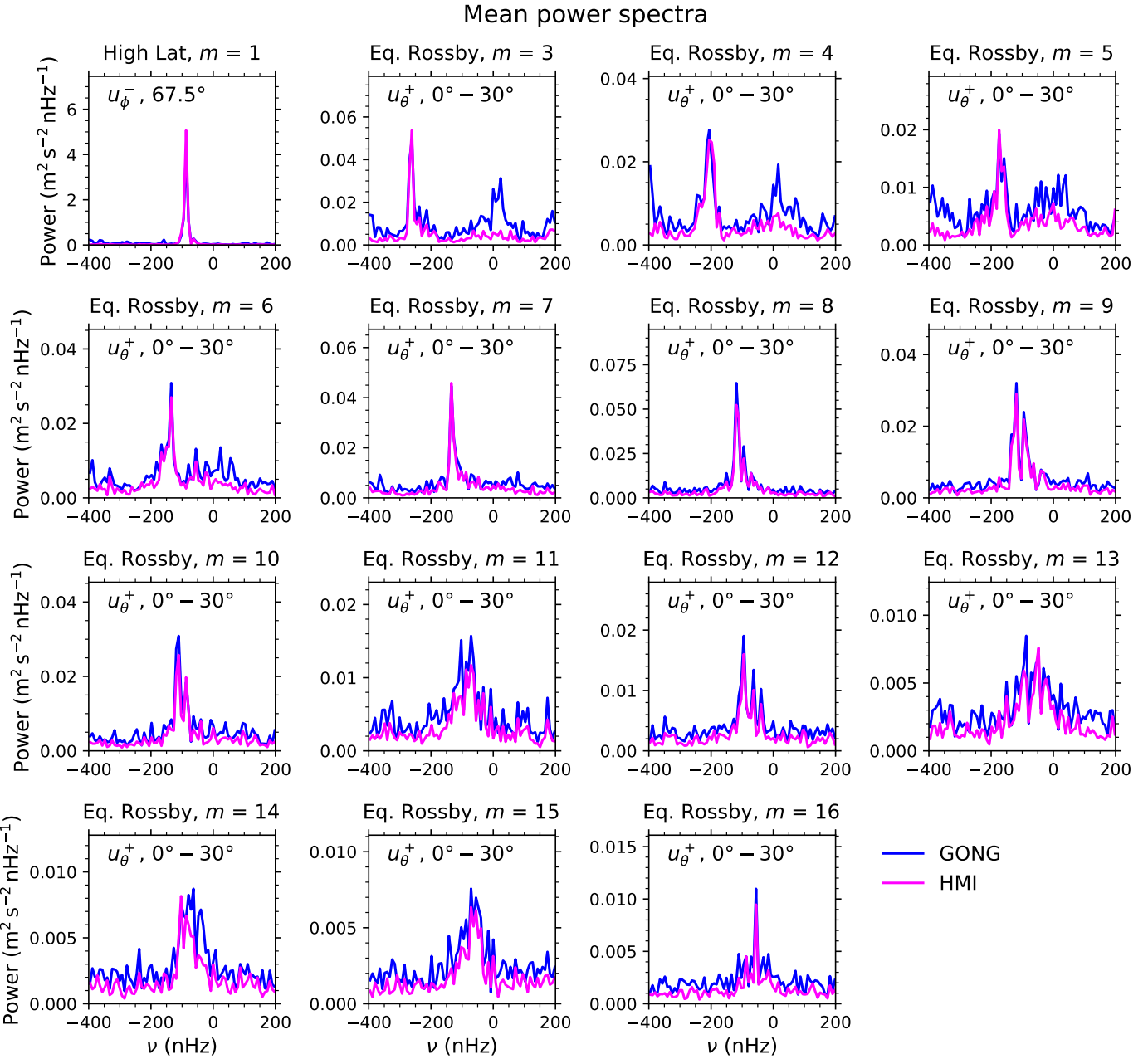


Fig. C.1: Mean power spectra $P_m(\nu)$ of u_ϕ^- at $m = 1$ and of u_θ^+ at $3 \leq m \leq 16$ showing the HL and ER modes respectively. They are computed from HMI (magenta) and GONG (blue) for the period 2010.5–2022.5.

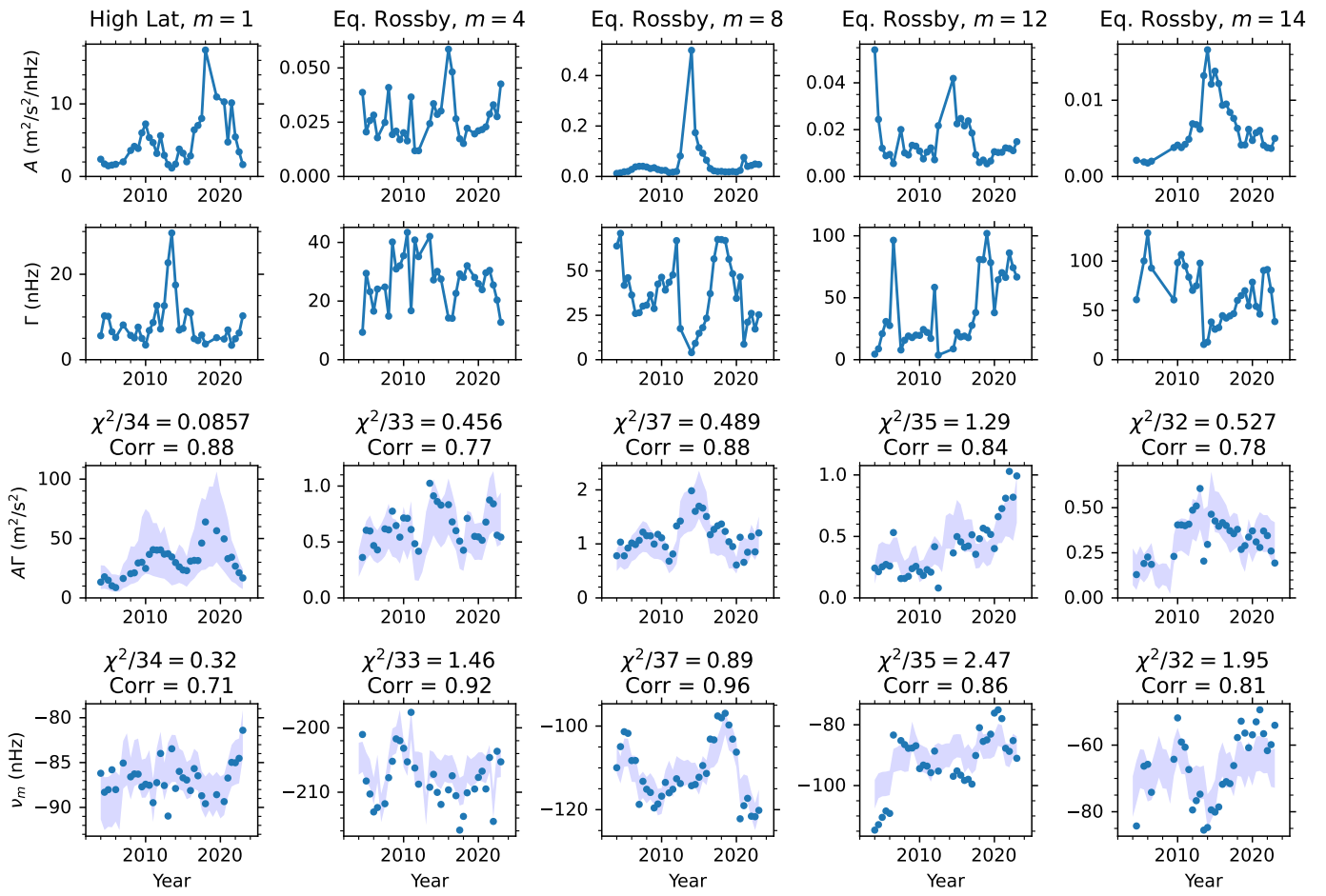


Fig. C.2: Mode parameters (including linewidths) for $m = 1$ high-latitude mode and $m = 4, 8, 12$, and 14 Rossby modes from Lorentzian fits. The dots in rows 1, 2, and 4 show the heights (A_m), full widths at half maximum (Γ_m), and mode frequencies (ν_m) obtained for each four-year time segment by fitting Lorentzian profiles to the data. The dots in the third row show the corresponding products $A_m \times \Gamma_m$, which provide a measure of the mode power inferred from the fits. In rows 3 and 4, shaded areas are included to illustrate the consistency with measurements obtained using the more robust method described in Section 3.2 (see Eqs. 5 and 6). The χ^2 values quantifying the differences between the two methods, as well as the corresponding correlation coefficients, are indicated in the plots.

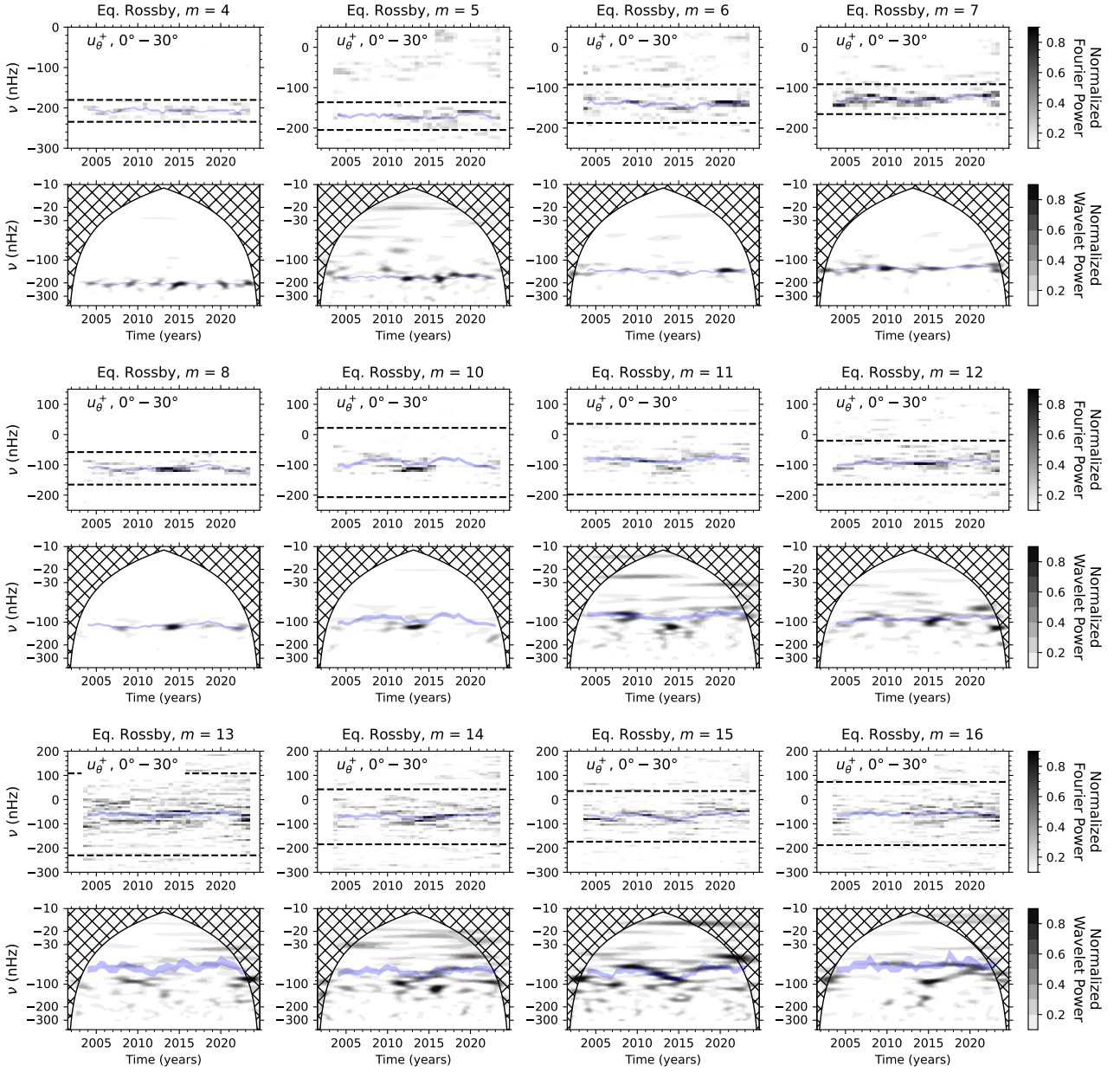


Fig. C.3: Similar to Fig. 5, but for the remaining modes.